Journal of large-scale research facilities

Journal of large-scale research facilities, 10, A191 (2026) http://dx.doi.org/10.17815/jlsrf-10-191

Published: 08.06.2026

The Cryogenic Ludwieg-Tube Göttingen (KRG) of the German Aerospace Center (DLR)

German Aerospace Center (DLR)
Institute of Aerodynamics and Flow Technology*

Scientists:
- Dr. Stefan Koch, stefan.koch@dlr.de
- Dr.-Ing. Henning Rosemann, henning.rosemann@dlr.de
- Dr. Alexander Wagner, alexander.wagner@dlr.de

Abstract:

The Cryogenic Ludwieg-Tube Göttingen (KRG) of the German Aerospace Center (Deutsches Zentrum für Luft- und Raumfahrt, DLR) is a Ludwieg-tube type of wind tunnel designed for high Reynolds number research in transonic flow. Temperatures down to 120 K and stagnation pressures up to 1 MPa are realised to achieve Reynolds numbers of up to $Re = 60 \times 10^6$ (2–D) based on a model chord of 150 mm while providing an exceptionally low turbulence level due to its design.

The Cryogenic Ludwieg-Tube Göttingen (KRG), in conjunction with the European Transonic Windtunnel (ETW), constitutes the exclusive aerodynamic infrastructure in Europe capable of achieving transonic flow at Reynolds numbers representative of full-scale flight conditions for modern transport aircraft. The KRG serves as a cornerstone of contemporary and future aeronautical research into high-Reynolds-number transport aircraft aerodynamics. It provides an economically efficient platform for the maturation of measurement techniques tailored to the rigorous demands of cryogenic test environments. Major research topics focus on drag reduction by laminar-turbulent boundary layer transition control and cavity flows for future aircrafts.

The present paper provides an overview over the Ludwieg-Tube concept and describes the design and operation of the facility as well as the main components with special emphasis on the 2–D adaptive wall test section and the adaptation method, based on Rosemann (1996). Furthermore, an overview on typical measurement techniques and selected research topics is provided.

*Cite article as: DLR Institute of Aerodynamics and Flow Technology. (2026). The Cryogenic Ludwieg Tube Göttingen (KRG) of the German Aerospace Center (DLR). *Journal of large-scale research facilities, 10*, A191. http://dx.doi.org/10.17815/jlsrf-10-191

1 Introduction

During the conceptualization of a new transonic high-Reynolds-number facility at DLR Göttingen, the Ludwieg-Tube principle was selected as the foundational architecture, Ludwieg (1955). The simple design was chosen for a number of good reasons. It keeps capital costs low and promises high flow quality due to the lack of many components typically causing disturbances in conventional wind tunnels, e.g. fans, turning vanes and meshes.

Because of the intermittent working principle, the costs for cryogenic operation, mostly determined by the consumption of liquid nitrogen, can also be kept small compared to continuously running wind tunnels. An inherent limitation of the Ludwieg-Tube principle is the constrained steady-state test duration, which necessitates the use of high-frequency or rapid-response measurement techniques.

The KRG was first equipped with a slotted wall test section. Tests and calibration runs were carried out to verify the concept and evaluate the performance of the KRG in the full range of operating temperatures. Later, a second test section with 2–D adaptive walls was designed and manufactured to enhance the quality of experimental results by eliminating interferences from the top and bottom walls. The adaptive wall test section also allows to test larger models, further increasing the Reynolds number and adding some supersonic capability to the facility, Section 2.3.4. The installation was concluded in summer 1994. The operation of the adaptive wall test section with the corresponding adaptation method and corresponding calibration results will be depicted in Section 3.5.

Between 2021 and 2025, the KRG facility underwent a comprehensive modernization program involving the overhaul of critical subsystems, including the liquid nitrogen storage, primary hydraulics, and both pressure and data acquisition systems. These infrastructure enhancements, integrated with a modernized process controller, successfully doubled the daily testing capacity.

2 Design and operational characteristics

2.1 Operating Principles of a Ludwieg-Tube

A Ludwieg-Tube basically consists of a long storage tube, a converging nozzle followed by the test section, a valve, and a dump tank. The gas dynamic process of the facility is explained in Fig. 1 by means of a x,t–diagram. Initially, the storage tube including all components upstream of the valve are charged to the desired pressure p_c, whereas the dump tank is kept at atmospheric pressure or below. Upon the opening of the valve an expansion wave travels upstream into the tube accelerating the gas to a Mach umber M_1 which is determined by the area ratio of the tube and the sonic throat in the valve. Equally, the Mach number in the test section is given by the area ratio of the test section and the sonic throat. The effective run time is terminated by the time the expansion wave returns to the test section after being reflected at the end of the tube, and the valve is closed. Between these two passages of the wave, all flow parameters in the test section remain constant as long as viscosity effects can be neglected.
During the passage of the expansion waves, the stagnation temperature T_{01} and pressure p_{01} drop be- low the pre-test charge values (denoted by the index c), see Fig. 1.

Fig. 2 shows the ratios p_{01}/p_c, T_{01}/T_c, the Mach number in the tube, M_1, and the length $\Delta L/L$ of the gas column passing through the test section as functions of the test section Mach number M for a nozzle contraction ratio of 3.6 which applies to the KRG.

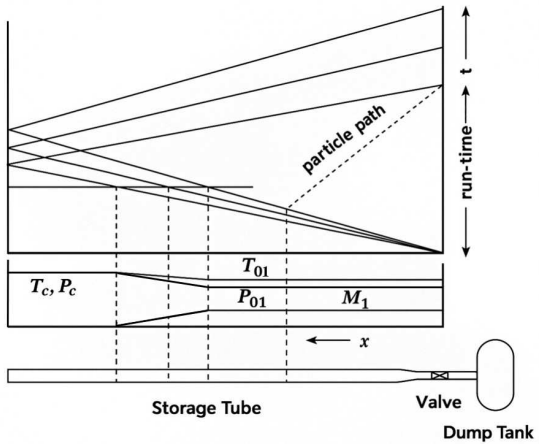

Figure 1: *x,t*–diagram of a Ludwieg-Tube (Rosemann, 1996)

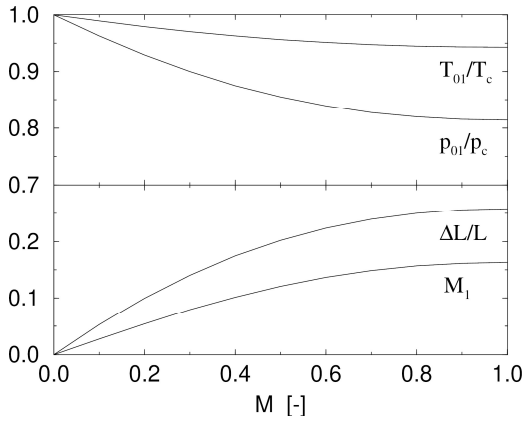

Figure 2: Characteristic flow parameters as function of the test section Mach number (Rosemann, 1996)

2.2 Specification

The basic requirement for the design of the wind tunnel was to obtain a Reynolds number of at least $Re = 50 \times 10^6$ on an airfoil model of 150 mm chord at transonic speeds. For an adaptive wall test section with flexible top and bottom walls the chord may be increased to 200 mm. From this, the main dimensions of the test section have been determined to be 400 mm width, 350 mm height and 2000 mm length. For wall mounted models a maximum stagnation pressure of 1 MPa is possible yielding the desired Reynolds numbers at a stagnation temperature of 120K. In Fig. 3 the *M, Re*–envelope is depicted for 2–D and 3–D models in comparison with the envelope of the ETW (3–D).

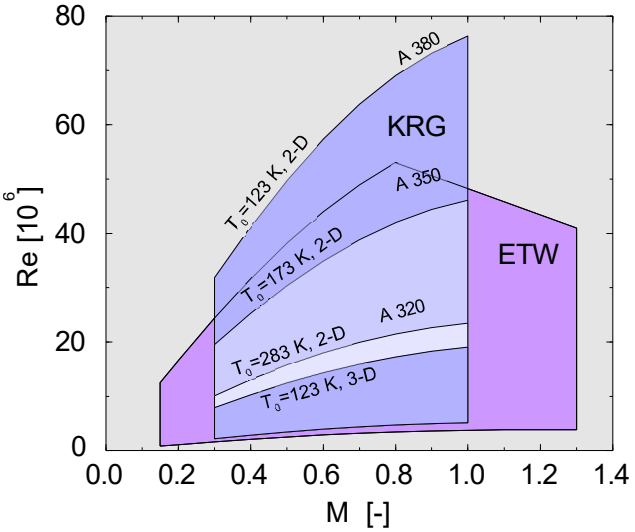

Figure 3: *M, Re*–diagram of KRG and ETW (based on Rosemann (1996))

The design goal of a 1 s run time at cryogenic temperatures resulted in a charge tube length of about 130 m. The unsteady boundary layer developing behind the expansion wave in the storage tube influences the flow quality in the test section. To counter that effect, the contraction ratio has been chosen to be 3.6, yielding a tube diameter of 0.8 m and a boundary layer displacement thickness at cryogenic temperatures of less than 4% of the tube radius.

2.3 The Present Ludwieg-Tube Design

2.3.1 General Description

A sketch of the general tunnel arrangement is given in Fig. 4. All components are mounted on rolls or sliding supports to account for the thermal contraction due to the cooling. The reaction forces are taken by two thrust stands located upstream of the gate valve and downstream of the bellows, the latter compensating for changes in length between these two points.

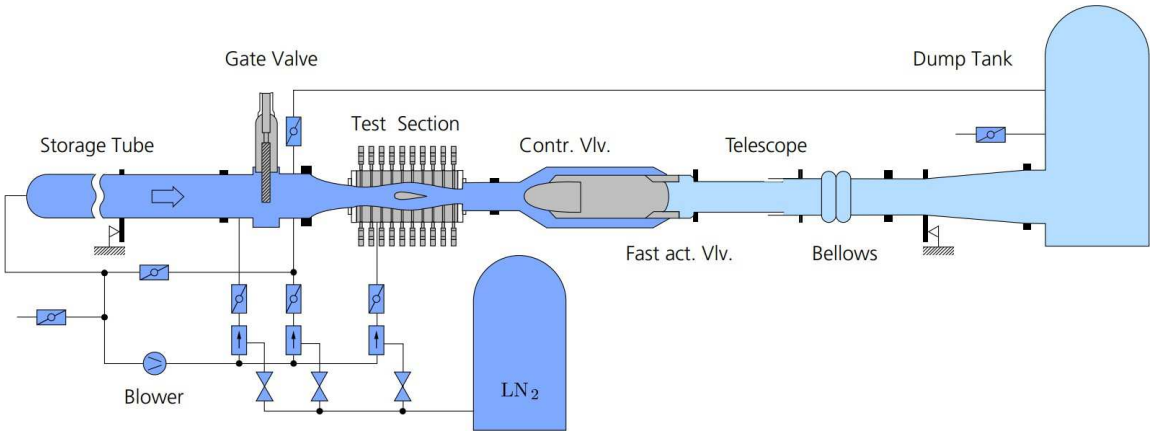

Figure 4: Schematic of the Cryogenig Ludwieg-Tube Göttingen (KRG)

The entire wind tunnel has been manufactured from stainless steel except the nozzle and the part downstream of the test section, which have been made of cast steel. The external insulation of the tube consists of an inner layer of mineral wool and an outer layer of polystyrene covered by a vapour barrier with a total thickness of 200 mm and an aluminum sheeting. A nitrogen purge system maintains the entire insulation at a low over-pressure to preclude entry of air or moisture. Figure 5 shows a photograph of the various layers of the tube insulation. All tunnel components are mounted on insulating wooden connections.

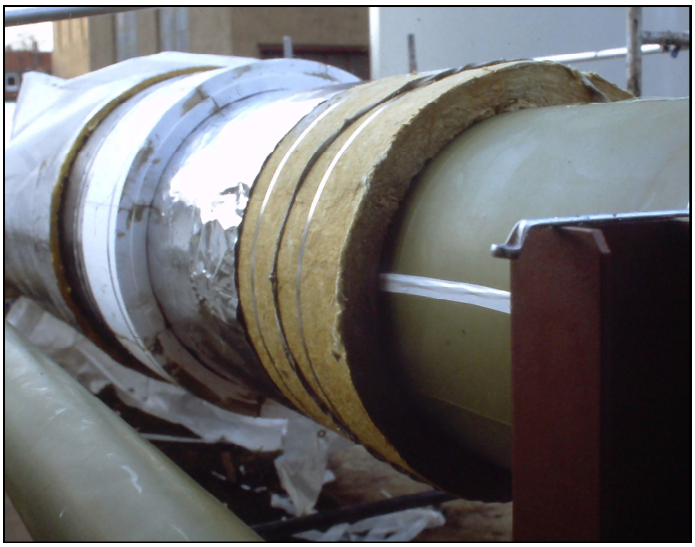

Figure 5: Insulation of the storage tube

The cool-down of the facility upstream of the fast-acting valve is conducted by circulating cold nitrogen by means of a blower using three feeding location and a return tube as indicated in Fig. 4. The gas is cooled before it enters the wind tunnel using liquid nitrogen. The convection speed in the main tube is high enough to achieve a uniform circumferential and longitudinal temperature distribution. Hence, a vertical temperature stratification is avoided and the temperature is constant during a run.

2.3.2 Gate Valve and Nozzle with Boundary Layer Bleed System

The gate valve upstream of the nozzle separates two charging and temperature conditioning loops: tube and test section (i.e. model) temperature can be adjusted independently offering the possibility of preconditioning the model to the correct temperature (or any other desired value). In addition, the gate valve prevents air from entering the tube when the test section is opened or removed. To compensate for the effects of the unsteady boundary layer in the tube on the flow quality in the test section, a boundary layer bleed system has been installed at the entrance of the nozzle, Fig. 6.

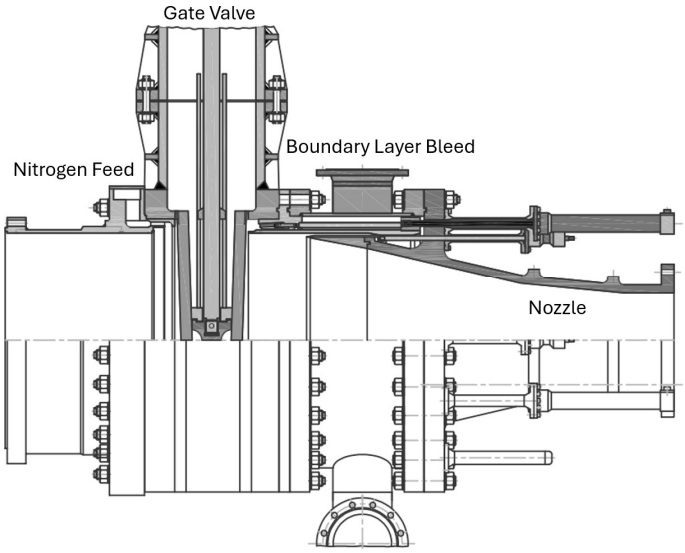

Figure 6: Gate valve and nozzle with boundary layer bleed

An upstream-actuated sliding sleeve, traversing from the nozzle's annular housing to bridge the gap between the gate and feeding ring, creates an annular orifice. This geometry facilitates the diversion of the boundary layer into a low-pressure plenum. The bleed mass flow rate can be controlled by adjusting the gap width according to the boundary layer displacement thickness. The fixed contour nozzle is made of austenitic cast steel. The cross section changes from a circle at the lip of the bleeding system to a rectangle of 400 mm by 350 mm at the exit.

2.3.3 Control Valve and Fast-Acting Valve

The run of a Ludwieg-Tube wind tunnel is controlled by the quick-opening valve which starts the flow and the sonic-throat diffusor which determines the Mach number in the test section. Both functions have been combined in the fast-acting control valve sketched in Fig. 7.

The valve assembly consists of an enlarged tube with a center body which contains two hydraulic actuators operating the control cone and the sleeve valve. The center-body is ventilated to the atmosphere and insulated on the inside; the temperature is controlled by electric heating. The control cone can reproducibly be positioned with an accuracy of 0.1 mm in order to adjust the test section Mach number with an accuracy of better than 0.001.

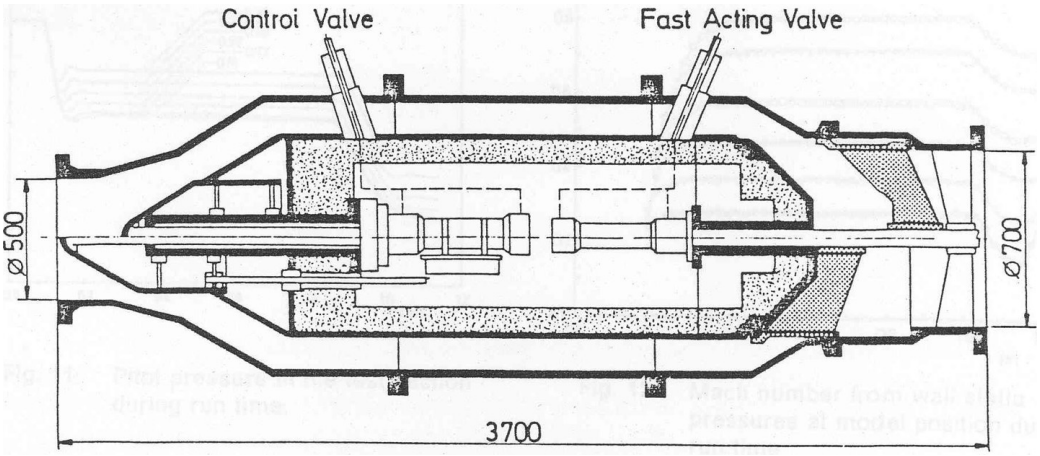

Figure 7: Sketch of control valve and fast-acting valve

Figure 8 shows the hydraulic actuator of the fast-acting valve in the center body. The contour of the control cone was re-engineered in 2007 to achieve higher transonic Mach numbers in the test section of the KRG (Gardner, 2007). The sliding cylinder at the rear of the valve starts the flow. The opening time can be adjusted to be less than 0.1 s.

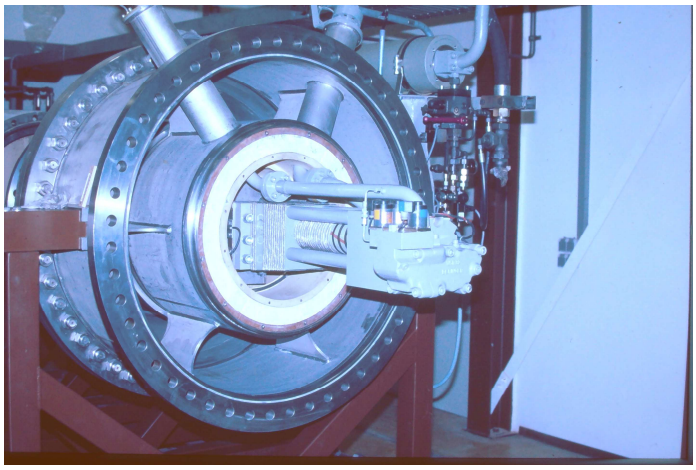

Figure 8: Hydraulic actuator of the fast-acting valve

2.3.4 The Adaptive Test Section

The adaptive wall test section can be easily opened via quick locking devices at the upstream and the downstream end of the test section and therefore grant a fast access to the wind tunnel model. The pressure shell of the adaptive wall test section is circular, but here it consists of four sectors to be clamped together, thus alleviating the assembly of the flexible walls. A longitudinal section and a cross sectional view is sketched in Fig. 9.

The flexible walls are made of glass and carbon fiber epoxy with a thermal expansion coefficient matching steel and can be adjusted by means of 19 jacks each operated by servomotors outside the wind tunnel shell under ambient conditions. The jacks are electrically heated to avoid damage to the seals due to ice building up on the moving parts. The maximum deflection of the flexible walls is ±45 mm. This allows also to use the upstream part of the wall as an extension of the nozzle with a convergent and a divergent section, such that the Mach number range of the facility can be extended to $M_\infty \approx 1.5$.

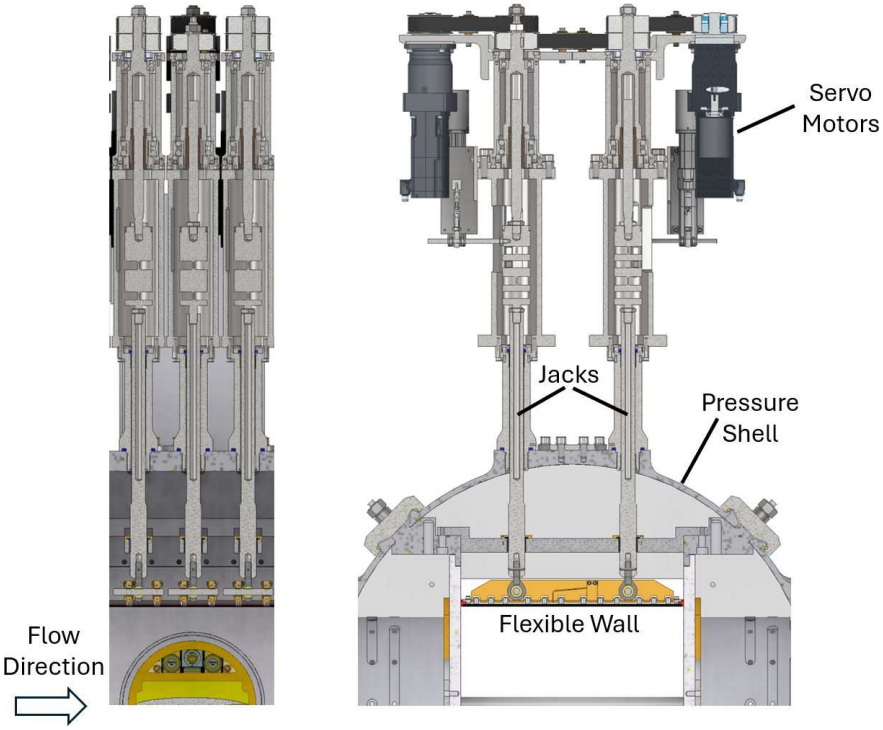

Figure 9: Sketch of the adaptive wall test section

In this case the model will be installed at a second mounting position 450 mm further downstream of the usual position, which is at approximately $x/l = 0.5$ in the test section. A photograph of the interior of the test section with the deflected walls is given in Fig. 10.

The servomotors are connected to the flexible walls through an additional gear box with a 10:1 gear ratio and self-locking spindles. Thereby all motors can be switched off during the experiment to eliminate the chance of disturbing other sensor signals by possibly noisy electronic servomotor power supplies. The control of the adaptive walls and the adaptation scheme is described below in Sec. 3.4 and 3.5.

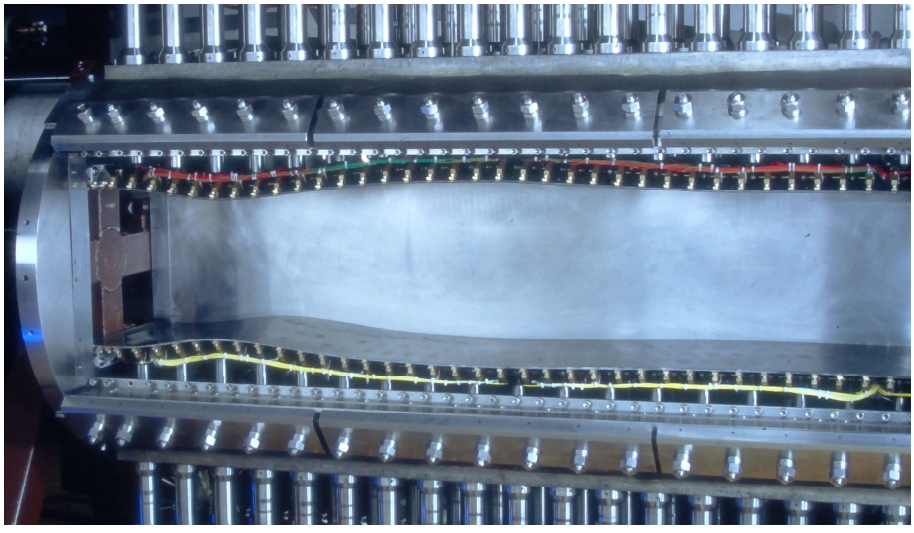

Figure 10: Adaptive walls of the test section (side wall removed)

3 Wind Tunnel Control and Data Acquisition/Evaluation

3.1 Operation and Control

All functions that are necessary to run the wind tunnel and vital to the safety of the facility are controlled by a "Simatic" process control computer, installed in the year 2025. This includes the hydraulic and pressurized air supply stations, the blower, temperature and pressure in the facility, the supply with gaseous and liquid nitrogen, and the various valves shown in Fig. 4. The oxygen level is monitored in the building for safety reasons.

Figure 11 shows the scientific workstation and the monitors connected to the two redundant PCs which are linked to the "Simatic" process control computer operating the KRG. Pressure is regulated automatically while the cool-down process and the temperature are controlled by the tunnel operator. The flow is initiated by opening the fast-acting valve for a specified duration.

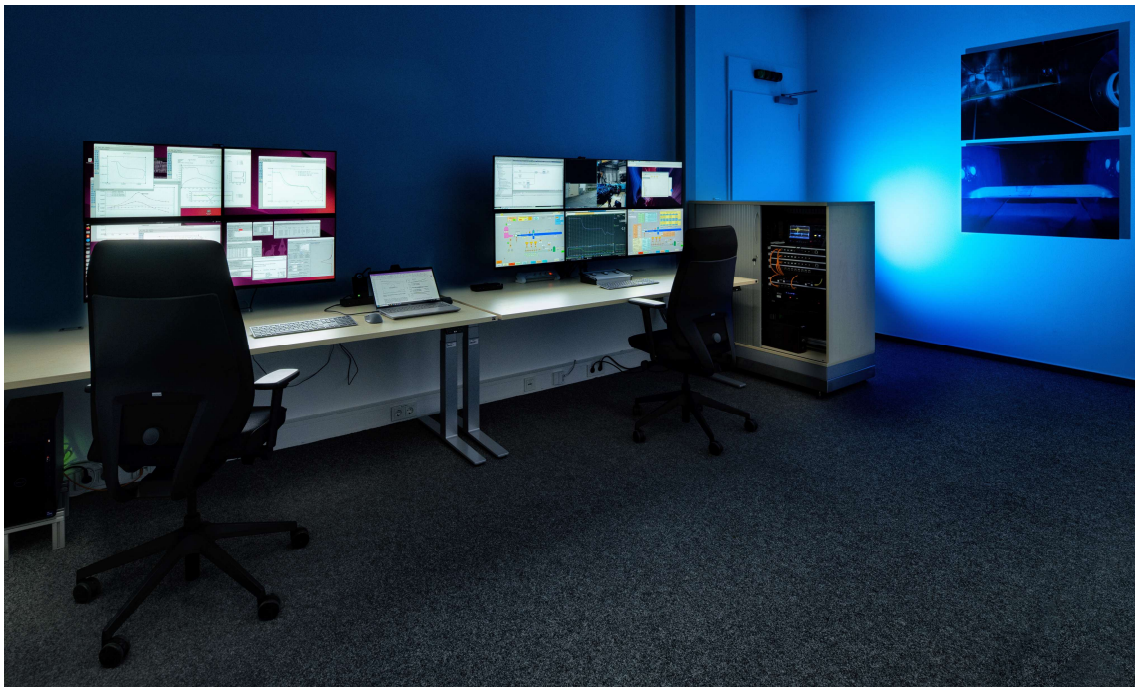

Figure 11: Scientific workstation and control display panels in the control room

3.2 Instrumentation and Data Acquisition

The distribution of the static pressure at the flexible upper and lower walls and the downstream left side wall of the test section is measured as well as some reference values of total pressure and temperature of the incoming flow. In addition the total pressure and the static pressure are scanned using a rake and a built-in airfoil model, respectively. A "DTC Initium System" equipped with temperature compensated "PSI ESP-32HD" and "PSI ESP-64HD" modules with a range of 45 psi is used. The nominal accuracy of the modules is specified as ±0.05% FS. The sampling rate of the "DTC Initium System" is typically 100 Hz/channel.

The reference pressure and the total pressure are measured with WIKA differential pressure sensors "P-30" (working range depending on charge pressure 250, 400, 600, 1000 or 1600 kPa) with an accuracy of ±0.05% FS. The sampling rate is 1 kHz/channel, using a 24-bit "Dewetron"-system for data acquisition.

Typically. the data is averaged over a time window of 0.1 s at the end of the run time to determine the mean value of the different pressures and coefficients. The "Dewetron"-system is also used for other sensors which have to be sampled at higher rates, like fast pressure transducers or hot-films. The test results are typically obtained within a few seconds after the run and are made available on a screen, as shown in Fig. 12.

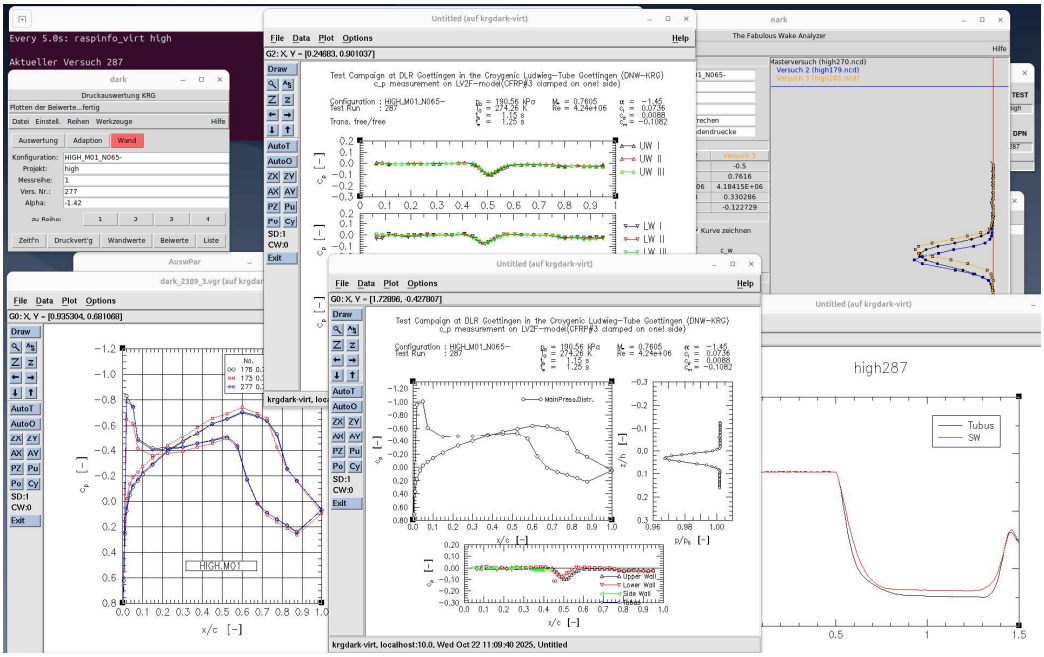

Figure 12: On-line data analysis

3.3 Airfoil Drag Measurements

A horizontally and vertically movable rake on a sting is positioned in the test section downstream of the 2–D model. The rake is equipped with 87 pitot probes having a length of 50 mm and a spacing of 2 mm, covering a height of 172 mm (Fig. 13). The distance of the probes from the model's trailing edge is typically 400 mm, presuming a model chord of 150 mm.

Figure 13: Wake rake with 87 pitot probes

The rake is not provided with static pressure probes, so the static pressure is measured on the upper and lower wall of the test section at the streamwise position of the rake. The static pressure is then interpolated to the position of the rakes pitot probes. Using the momentum theorem the drag coefficient c_d of the installed 2–D model can be calculated with these measured quantities of the flow.

3.4 Instrumentation and Control of the Adaptive Wall Test Section

When the adaptive wall test section was put into operation in 1995, the layout of the control of the flexible walls was guided by the fact that during the short test time no adjustment of the walls would be necessary (and possible). Therefore multiplexers were used both to connect the stepper motors to one electronic power unit for each wall and also to measure the outputs from the positional sensors, thereby reducing costs considerably. The drawback of this solution was that the stepper motors were driven one after the other. And after all motors moved the 19 jacks by 2 mm maximum in one step, the position sensor system measured the actual shape of the wall, to ensure that the mechanics did not jam. This time consuming procedure was repeated until the final shape of the wall was met. In 2025 the drive system of the adaptive wall was exchanged and the stepper motors were replaced by servomotors. The position sensing system of the walls was also renewed and is now a combination of internal angular sensors within the servomotors on the one hand and a magnetostrictive linear sensor system on the other hand. While the new motors and the sensor system of the adaptive wall is now connected to the "Simatic" process control computer and every servomotor has its own power unit, it is possible to move the adaptive walls as a whole and at the same time the positioning of the wall is tracked. Therefore the time needed to adapt the walls is reduced dramatically and the efficiency of the KRG is increased. Limited by the mechanical construction, the position of the wall is set and determined with an accuracy of about 0.1 mm. For the adaptation scheme described in the next section the wall contour and the wall pressure distribution have to be known. Therefore, both top and bottom wall are equipped with three stream-wise rows of 42 pressure tabs in each row. The three parallel rows provide also the spanwise information necessary for 3–D adaptation schemes.

3.5 The Adaptation Procedure

Since the flexible walls of the KRG can not be adjusted during the short run time, using an iterative adaptation procedure would require a large number of runs to produce one interference-free result. Therefore, a single step method based on the Cauchy's integral formula:

$$f(z) = \frac{1}{2\pi i} \oint_C \frac{f(\zeta)}{\zeta - z} d\zeta \tag{1}$$

with:

$$\zeta = \xi + i\eta; \qquad f(\zeta) = U_C - iV_C \tag{2}$$

and:

$$z = x + iy; \qquad f(z) = U - iV \tag{3}$$

is applied for 2–D adaptation (Amecke, 1985). Equation (1) allows the computation of the velocity components U and V at any point (x, y) inside a closed curve $C(\xi, \eta)$ by integrating the velocity components U_C and V_C along C, see Fig. 14.

For adaptation purposes, the integration path C is chosen to consist of the upper and lower wall as well as of the inlet and outlet cross section of the test section, enclosing the model. Furthermore, it is assumed that the flow in the test section can be described as a superposition of the velocity field induced by singularities representing the model and of singularities representing the wall interferences. Then Eq.(1) can be used to compute the wall induced velocities inside the test section because it can

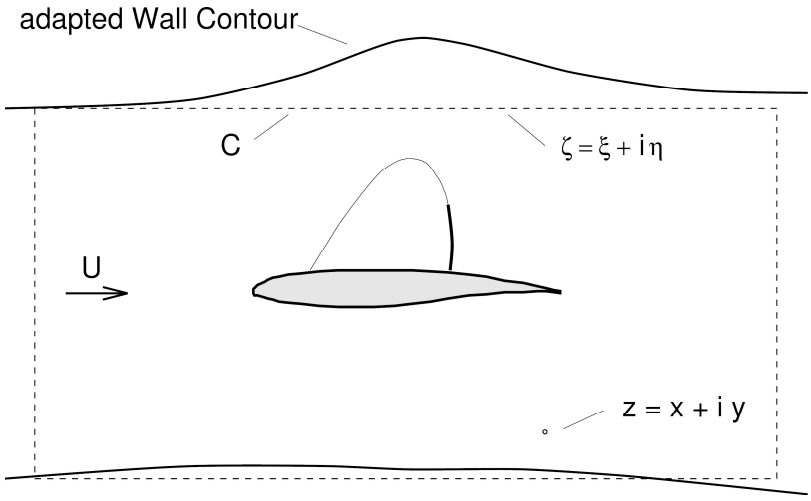

Figure 14: Wall adaptation based on Cauchy's integral formula (Rosemann, 1996)

be shown (Hurwitz, 1964), that singularities within C do not contribute to the value of the integral. So the result of Eq.(1) is only determined by those singularities located outside of C, representing the wall influence.

For an adaptation process first the velocity components U_C and V_C are determined from wall pressure measurements and the slope of the walls. For the in- and outflow conditions appropriate assumptions have to be made. Then, the wall-induced velocities at the position of the walls can be computed using Eq.(1). The wall influence is canceled by deflecting the wall by an angle of the same size as given by the wall-induced velocity components, but with opposite sign. The next run with the adjusted wall contours should give the interference-free results.

This method is limited to flows that can be described by the linearized potential equations, at least in the proximity of the walls. Compressibility effects are taken into account by the Prandtl-Glauert rule. It is therefore to be expected, that for flows with separated regions or large supersonic flow regimes and strong shocks the results will become less accurate. However, it was found that even though an interference-free wall contour is not achieved in a single step under all circumstances, the algorithm still converges, so that interference-free results can be obtained for the prize of some additional runs.

The adaptation procedure was first tested with an empty test section, only equipped with a rake. Figure 15 shows the wall contours and wall pressure distributions before and after the adaptation. The first run with straight walls shows the acceleration of the flow due to the boundary layer development at the test section walls. At about x = 1.4 m the displacement effect of the rake mounted along the test section axis becomes visible.

Using the pressure distribution as input for Eq.(1), the wall displacement shown in Fig. 15 was computed and the wall adjusted accordingly. The second run resulted in a nearly constant pressure distribution along the walls. It might be surprising, that although no correction for the boundary layer displacement thickness had been applied, a constant pressure distribution was obtained. This is obviously the case because the influence of the boundary layer is mostly noticeable in the flow acceleration. Using the slope of the real wall instead of the one corrected with the boundary layer displacement thickness to compute the velocity components U_C and V_C for Eq.(1) from the pressure distribution is nearly exact for U_C and only leads to small errors in V_C, since the boundary layer is growing only slowly. Tests show, that taking into account a reasonably estimated boundary layer displacement thickness changes the computed wall contour only by about 0.2 mm at the position of the model at x = 1 m.

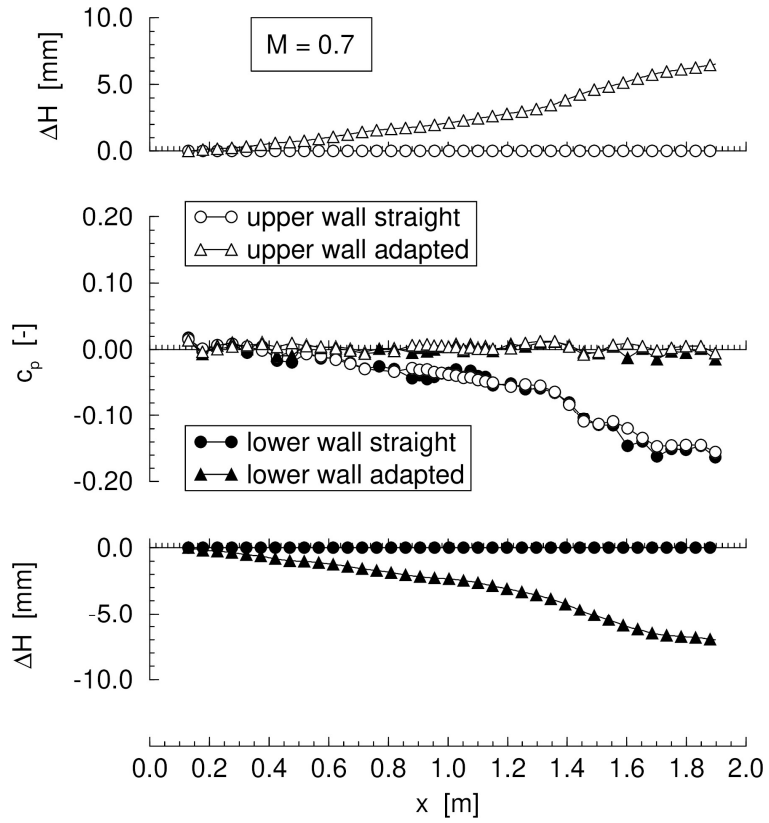

Figure 15: Adaptation of the empty test section (Rosemann, 1996)

An example for a wall adaptation with model is shown in Fig. 16. The pressure distributions at the model and at the walls show large differences between the first run carried out with straight walls and the fully adapted case, achieved with the second iteration. Very obvious is the velocity increase at the suction side of the model and the upper test section wall due to the straight channel, but, the flow at the walls is still subsonic ($c_p^* = -0.63$ for $M = 0.74$). The pressure distributions at the walls also show the acceleration of the flow before adaptation because of the growth of the wall boundary layers. Again, no boundary layer displacement effect was considered.

For these large wall displacements, adaptation is not achieved in one step. The first iteration brings the wall already close to the final contour, but a slight overshoot has to be corrected in a second step. A third iteration would require wall adjustments of less than 0.2 mm, such that the adaptation is considered to be complete after the second step. Lift changes by $\Delta c_L = 0.007$ and drag by $\Delta c_D = 0.0001$ from the first to the second iteration.

A representative example of the adaptation routine is provided in Fig. 17. Here, an α-sweep was carried out at constant Mach number with $\Delta\alpha = 0.5^\circ$. Only small adjustments of the wall contour are necessary from one point of the polar to the next and at these Mach numbers full adaptation is achieved in one step up to moderate lift conditions.

Figure 17 shows a high lift case, for which two iterations are necessary to reach a converged solution of the wall contour. Further adjustments remain below 0.2 mm. It can be seen, that the position of the shock is very sensitive to small changes of the wall contour, whereas the other regions of the pressure distribution remain nearly unchanged between the first and the second step.

The iteration is usually performed until further wall adjustments are within the mechanical tolerances of wall construction, or the changes of the results, e. g. the force coefficients are within the limits of the required accuracy given by Steinle & Stanewsky (1982). For the adaptation of the 2–D flexible wall for 3–D flow experiments other methods (e. g. Holst (1991)) are available and can be applied.

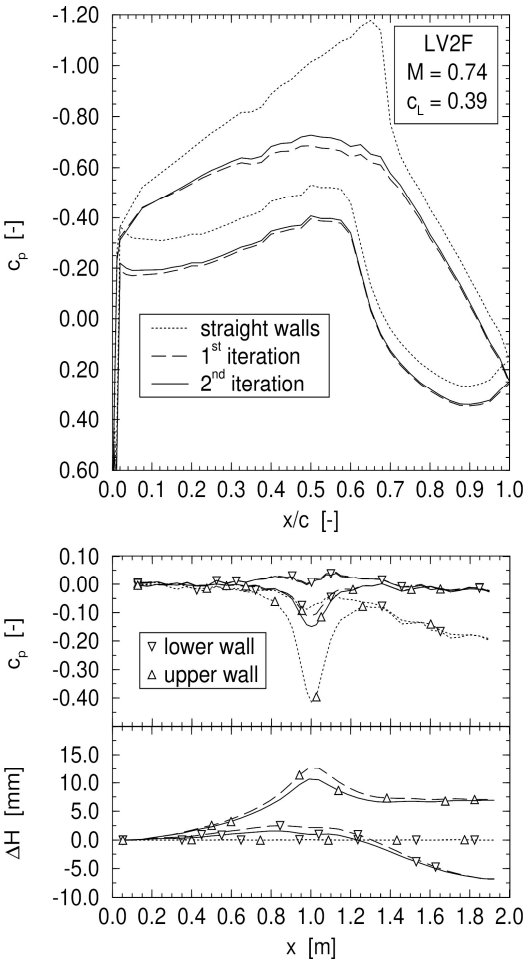

Figure 16: Adaptation starting from straight walls (Rosemann, 1996)

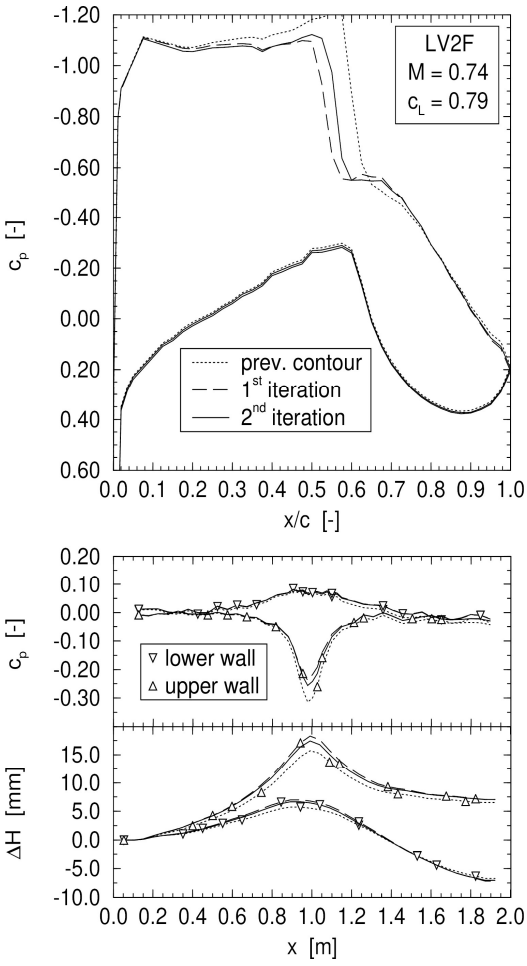

Figure 17: Adaptation starting from the previous point of an α-sweep (Rosemann, 1996)

4 Measurement Techniques Overview

4.1 Wall Temperature Measurements by Thermocouples

This technique exploits the difference in the heat transfer from the flow to the model between laminar and turbulent boundary layers. When the flow in a Ludwieg-Tube is started, the total temperature drops by a certain amount (cf. Fig. 1 and 2) and the wall underneath a turbulent boundary layer will adjust faster to the new flow temperature because of the higher heat flux yielding a measurable difference in the temperature gradient to the laminar region. This method was already applied in the T2 wind tunnel at ONERA, Toulouse, but had to be adapted to the short run time of the KRG (Schülein et al. (1998)).

For a first test, three thermocouples had been mounted 0.5 mm underneath the skin in the model wall with a thickness of 3 mm of the laminar type airfoil model DA-LVA 1Ae, designed and built by DASA (now AIRBUS).

Figure 18 shows the temperature traces of the sensors located at 12.5%, 32.5% and 47.5% chord, respectively, for three different Reynolds numbers. Transition was tripped at 48% chord, just downstream of the third sensor. When the flow starts at about $t \approx 0.2$ s, very little temperature change over the run time is measured for $Re = 4.6 \times 10^6$. At higher Reynolds numbers, larger gradients are observed starting at the most downstream sensor, until at $Re = 11.8 \times 10^6$ all three sensors indicate a stronger heat flux. This development is an indication for the forward movement of the transition point in this Reynolds number range.

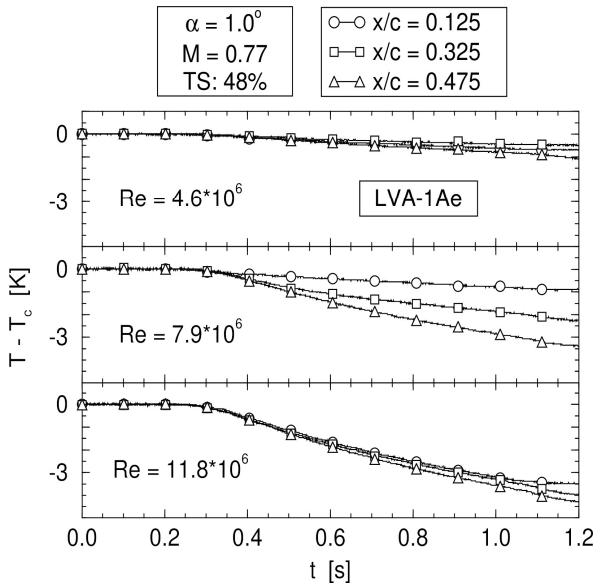

Figure 18: Transition detection by wall temperature measurement (Rosemann, 1996)

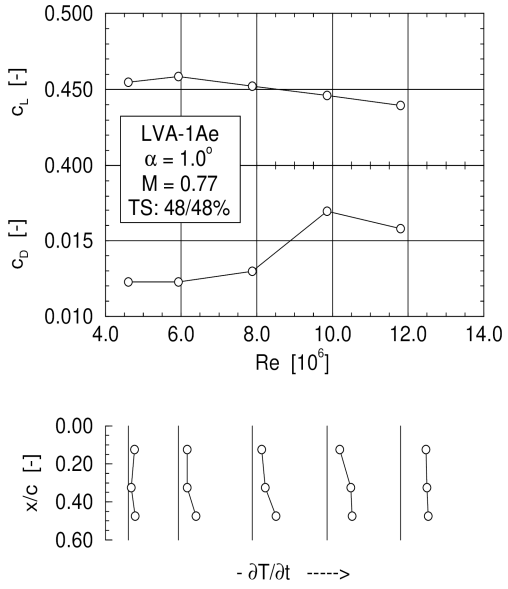

Figure 19: Lift, drag and heat-transfer as function of Reynolds number (Rosemann, 1996)

In Fig. 19 the lift and drag coefficients are plotted along with the temperature gradients versus Reynolds number, showing the correlation between the forward movement of the transition and the increase of the drag coefficient between $Re = 8 \times 10^6$ and $Re = 10 \times 10^6$. For more precise measurements the chordwise resolution can be improved by placing more sensors in the model.

4.2 Surface Hot-Films on the Model Wall

Hot-film measurements in aerodynamics are based on convective heat transfer from a small electrically heated sensor to the surrounding flow. A thin metallic film, deposited on a substrate, is maintained at constant temperature (Constant Temparature Anemometry, CTA). As fluid velocity changes and therefore the wall shear stress, the convective cooling rate changes, altering the electrical power required to keep the film at its operating condition. Hot-film sensors are widely used for boundary-layer studies, transition detection, turbulence measurements, and unsteady flow investigations.

A LV2F laminar type airfoil was equipped with a hot-film sensor array to investigate the transition behaviour on a 2–D profile in the KRG (Fig. 20). The very thin boundary layers created by the high Reynolds number flow and low test temperatures require a specialized hot-film system. The hot-film sensor system was directly deposited on the model surface and is characterised by its low surface roughness, guaranteeing a disturbance free transition measurement.

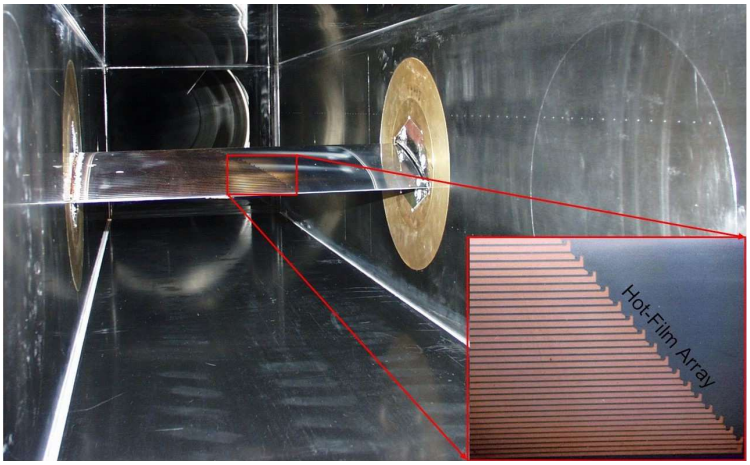

Figure 20: LV2F-airfoil with a hot-film array in the adaptive test section of the KRG. Upstream view into the Ludwieg-Tube

The point of transition, length of intermittent flow, and a range of other boundary layer properties could be extracted from the hot-film data. This allowed the characterisation of the temperature influence on transition at constant Mach and Reynolds number (Fig. 21). In the meantime it was possible to proof that hot-films already coated on a Kapton® foil can be used for boundary layer measurements on a wind tunnel model in the KRG providing additional flexibility (Dimond, 2024).

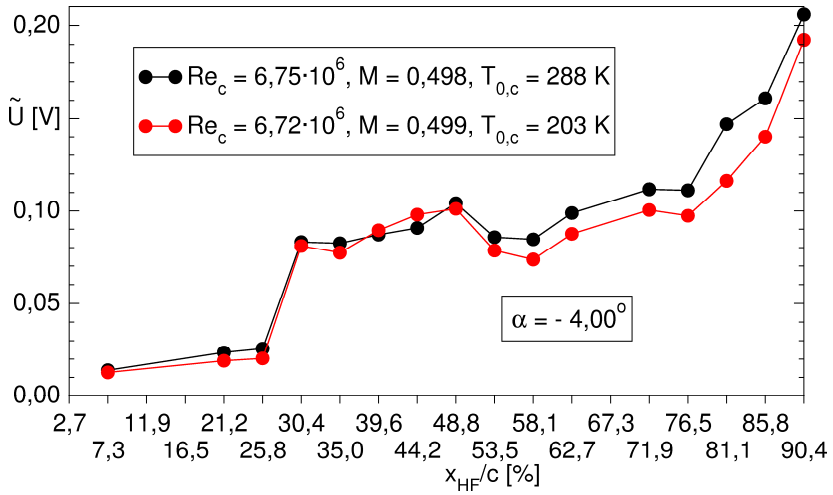

Figure 21: Transition location on the LV2F laminar type profile by means of the hot-film rms signal. The data shows the independence of the transition location (x/c=30%) to different flow temperatures in the KRG (Koch, 2004)

4.3 Temperature Sensitive Paint and Pressure Sensitive Paint

Temperature-Sensitive Paint (TSP) is an advanced optical technique used primarily in experimental aerodynamics to measure surface temperature distributions with high spatial resolution. Unlike traditional discrete sensors such as thermocouples or hot-films, which provide data only at distinct points, TSP allows for the continuous mapping of temperature fields over complex geometries.

The fundamental working principle relies on the photophysical properties of luminescent molecules, known as luminophores, which are added to a polymer binder and applied to the test surface. When the TSP coating is illuminated by a light source of a specific wavelength (typically in the ultraviolet

or blue spectrum) the luminophores are excited to a higher energy electronic state. These molecules subsequently return to their ground state by emitting photons at a longer wavelength, a process known as luminescence. The critical mechanism governing TSP is thermal quenching. As the temperature of the binder matrix increases, the probability of the excited molecules returning to the ground state via non-radiative pathways increases. Consequently, the intensity of the emitted light decreases as the surface temperature rises.

Temperature-Sensitive Paint (TSP) is particularly valued in wind tunnel testing for its ability to spatially resolve the boundary layer transition from laminar to turbulent flow (Fey & Egami, 2007; Risius et al., 2018). The detection relies on the direct relationship between local skin friction and convective heat transfer, known as the Reynolds analogy. In a typical setup, the wind tunnel model is actively heated to create a temperature difference between the surface and the freestream flow. In the KRG a temperature drop at the beginning of a test run (see Fig. 1) results in a natural temperature difference between the flow and the thermal inert steel model which simplifies the application of TSP (Fig. 22).

Figure 22: Illuminated TSP-model in the KRG, upstream view on the model's trailing edge

Due to the fact that turbulent flows induce significantly higher heat transfer rates than laminar flows, the surface temperature evolves differently in these two regimes. The turbulent region experiences a higher rate of heat flux, resulting in a distinct surface temperature difference compared to the laminar region. Since the TSP coating's luminescence intensity is inversely proportional to temperature, this thermodynamic disparity creates a strong optical contrast. The transition front manifests as a sharp gradient in the processed images, allowing to instantaneously visualize the topology of the transition line. At KRG, measurements have been conducted using time-resolved Temperature Sensitive Paint (iTSP) at frequencies of several 10 kHz (Dimond, 2024).

While TSP utilizes thermal quenching to map heat transfer, Pressure-Sensitive Paint (PSP) relies on the distinct photophysical mechanism of oxygen quenching to measure surface pressure. The PSP coating comprises luminescent molecules dispersed within a gas-permeable polymer binder. When the coated surface is illuminated with light of a certain wavelength, the luminophores are excited to a higher energy state. Unlike in TSP, where heat drives non-radiative decay, in PSP, the excited molecules are deactivated primarily through collisions with oxygen molecules. The oxygen concentration within the

binder is again directly proportional to the external static pressure. Consequently, regions of higher air pressure introduce more oxygen into the layer, increasing the rate of quenching and thereby reducing the intensity of the emitted light. Conversely, low-pressure areas, such as suction peaks, appear brighter. This technique allows to generate continuous global pressure maps, visualizing complex flow features like a shock wave or a separation bubble. Considering the fact that oxygen gas has to be injected into the pure nitrogen gas atmosphere of the KRG, Klein et al. (2020) showed the capability of time resolved iPSP to measure shock oscillations on a laminar type airfoil at cryogenic conditions in the KRG test section, see also Klein (2022).

The maturation of Temperature-Sensitive Paint (TSP) and Pressure-Sensitive Paint (PSP) techniques for high-Reynolds-number cryogenic environments has been extensively facilitated by dedicated test campaigns within the KRG facility. Technological refinements to both TSP and PSP are systematically validated within the KRG before their deployment at the European Transonic Windtunnel (ETW) in Cologne. Consequently, among other research scopes, the KRG serves as a primary testbed for instrumentation maturation, ensuring the reliability of optical diagnostics prior to large-scale campaigns at the ETW.

4.4 Particle Image Velocimetry

Particle Image Velocimetry (PIV) is a non-intrusive optical diagnostic technique for quantitative velocity-field measurements in aerodynamic flows. The fluid is seeded with tracer particles of sufficiently small Stokes number to ensure dynamic response to the carrier phase. A pulsed laser forms a thin light sheet that illuminates a planar section of the flow, and two exposures are recorded with a precisely controlled interframe time. The particle image displacement within interrogation regions is evaluated using statistical cross-correlation, yielding a two-dimensional displacement vector field. Division by the known time interval provides the instantaneous velocity field.

First tests with PIV were done at the Cryogenic Ludwieg-Tube on a S-duct intake on a flat plate as part of the DLR project "Diabolo" (Fig. 23, see also Section 5.5). Ice crystals were used as tracer particles and seeded the KRG's storage tube within a certain area. When the single test run started, the ice seeding moved through the test section along the test object at the proper instant of time, resulting in a adequate seeding distribution at the installed laser sheet. However, PIV remain challenging in such test environments.

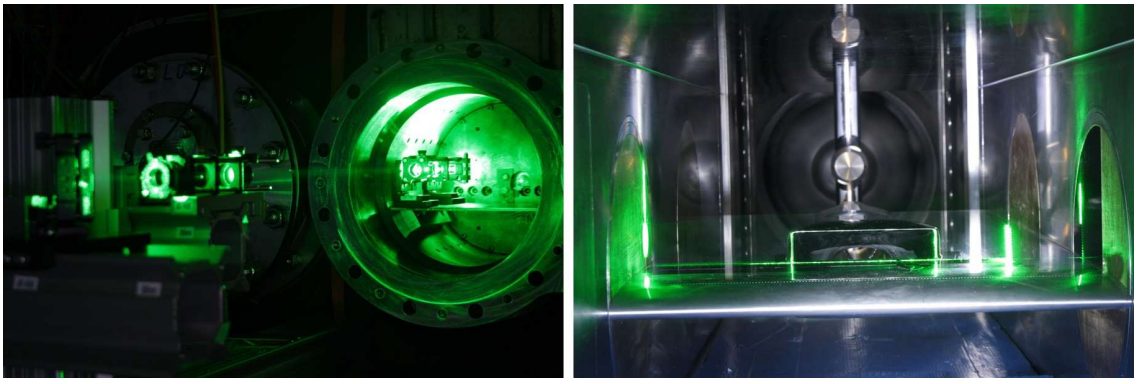

Figure 23: Left: PIV setup in the KRG test section; right: laser sheet positioned upstream of a rectangular intake above a flat plate

5 Research Topics Overview

5.1 Flow Quality

In addition to the simulation of the entire Reynolds number range, also the turbulence level of the wind tunnel's incoming flow has to be comparable to free flight conditions. The flow quality of the KRG is characterized by generally low turbulence levels, a feature attributed to the design of Ludwieg-Tube wind tunnels which lack the drive fans and turning vanes of continuous circuit facilities. Furthermore, the KRG demonstrates exceptionally low total temperature turbulence.

Flow quality measurements have been conducted in the KRG investigating the spatial development of single fluctuation quantities. The total pressure, static pressure, total temperature and mass flux were recorded in the test section and in the storage tube of the KRG (Koch, 2004). The dependence of the flow quality on the fluid temperature was of special interest, as an influence of the temperature is to be expected when the fluid is cooled down to 120 K to achieve flight Reynolds numbers (Fig. 24).

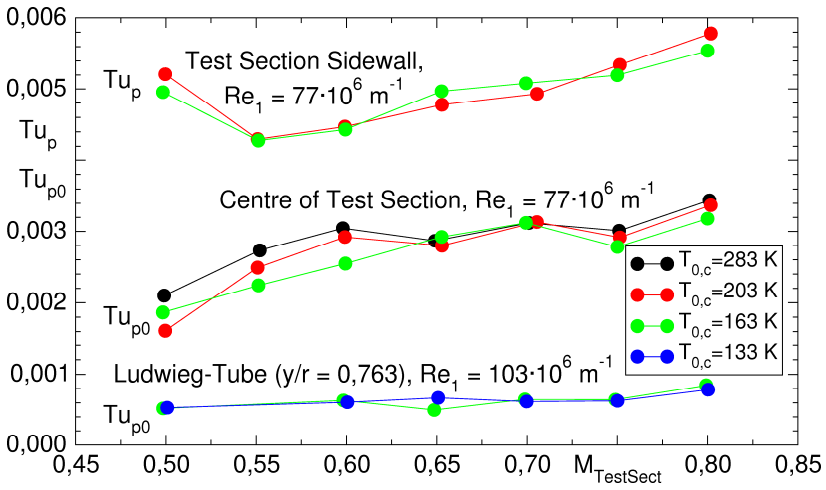

Figure 24: Influence of the wind tunnel charge temperature $T_{0,c}$ on different turbulence parameters in the KRG test section at varying Mach number and constant unit Reynolds number

5.2 Transition

As the Cryogenic Ludwieg-Tube in Göttingen is one of the few wind tunnels world wide that are capable of achieving flight Reynolds numbers of transport aircraft at transonic speeds, it is evident that the KRG is a preferred facility for boundary layer transition research. As the necessary similarity laws are met, the transition line measured on the wind tunnel model, with e.g. TSP, will correspond to the situation in flight. Due to the very good flow quality in the test section of the KRG, the laminar length of the boundary layer on the airfoil was measured up to 73% chord at $Re = 20 \times 10^6$ at transonic speeds as shown in Fig. 25.

The influence of surface irregularities on the boundary layer transition is of vital interest for the idea of a laminar wing transport aircraft. Several test campaigns have been conducted at KRG, as a basis for further investigations leading to the European flight test program BLADE (Breakthrough Laminar Aircraft Demonstrator in Europe, (Gibson et al., 2020)). While TSP is often applied to investigate the boundary layer status, hot-films have also been used at KRG to gain a deeper insight in the transition process. This expertise in hot-film measurements was transferred to flight tests in the scope of BLADE.

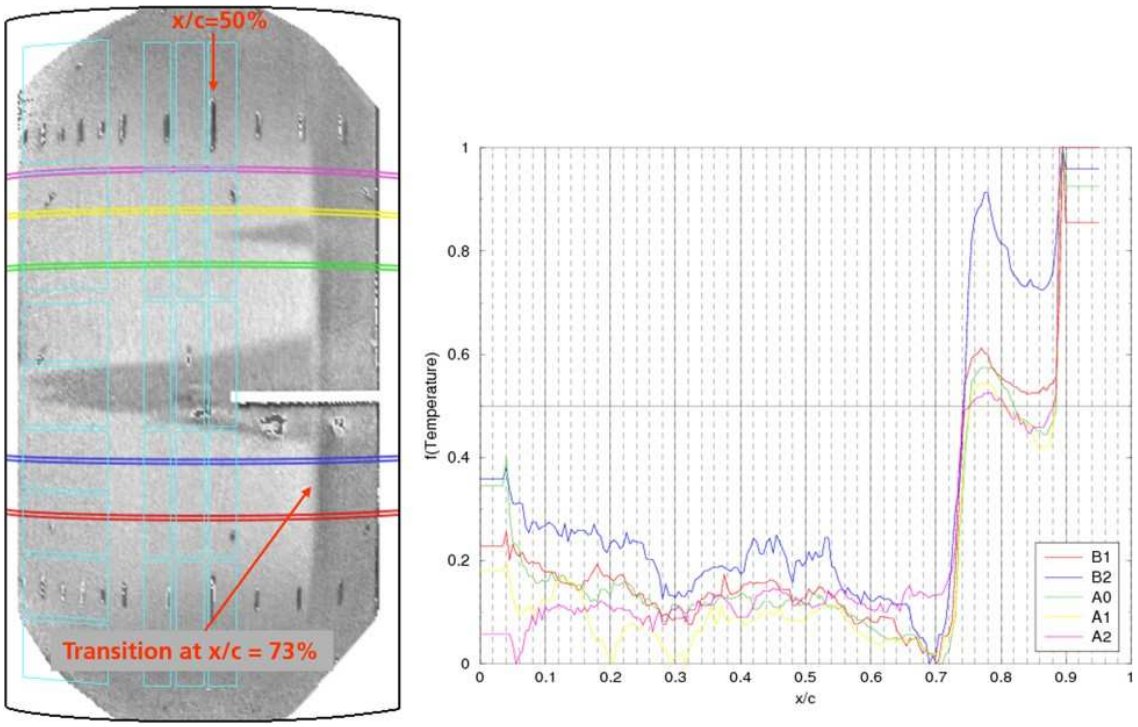

Figure 25: TSP grayscale representation of the upper surface of a 2–D profile measured at transonic speed and $Re = 20 \times 10^6$. Intensity distribution indicate the transition location at 73% chord length

5.3 Flow Control

Flow control in aerodynamics is dedicated to the manipulation of the flow field to achieve advantageous physical changes. The primary objectives of this intervention include e.g. the delay or total prevention of boundary layer separation, the mitigation of parasitic and induced drag, the enhancement of aerodynamic lift or specifically targeting the delay of transition from laminar to turbulent boundary layers.

Flow control strategies are broadly classified into passive and active measures. Passive flow control operates without external energy expenditure, employing fixed geometric modifications such as vor- tex generators (see also Section 5.5), riblets, or bumps. Conversely, active flow control necessitates localized energy deposition into the fluid medium. These advanced actuators introduce steady or unsteady perturbations, like steady suction, oscillatory blowing, synthetic jets, and plasma actuators. By modifying the near-wall flow, these methodologies enable airfoils to operate significantly beyond their conventional margins, offering improvements in the operational efficiency, maneuverability, and overall performance of advanced aircraft systems.

Among other test campaigns regarding flow control measures, e.g. on miniature trailing-edge devices, experiments were conducted in the KRG dealing with the influence of a shock control bump in combination with an active suction on a transonic airfoil to reduce the viscous drag as well as the shock induced drag (Koch, 2020). Using the combined flow control measures at a Mach number of $M = 0.765$ and a lift coefficient of $c_l = 0.63$, the drag was reduced about 24% compared to the datum airfoil profile Fig. 26.

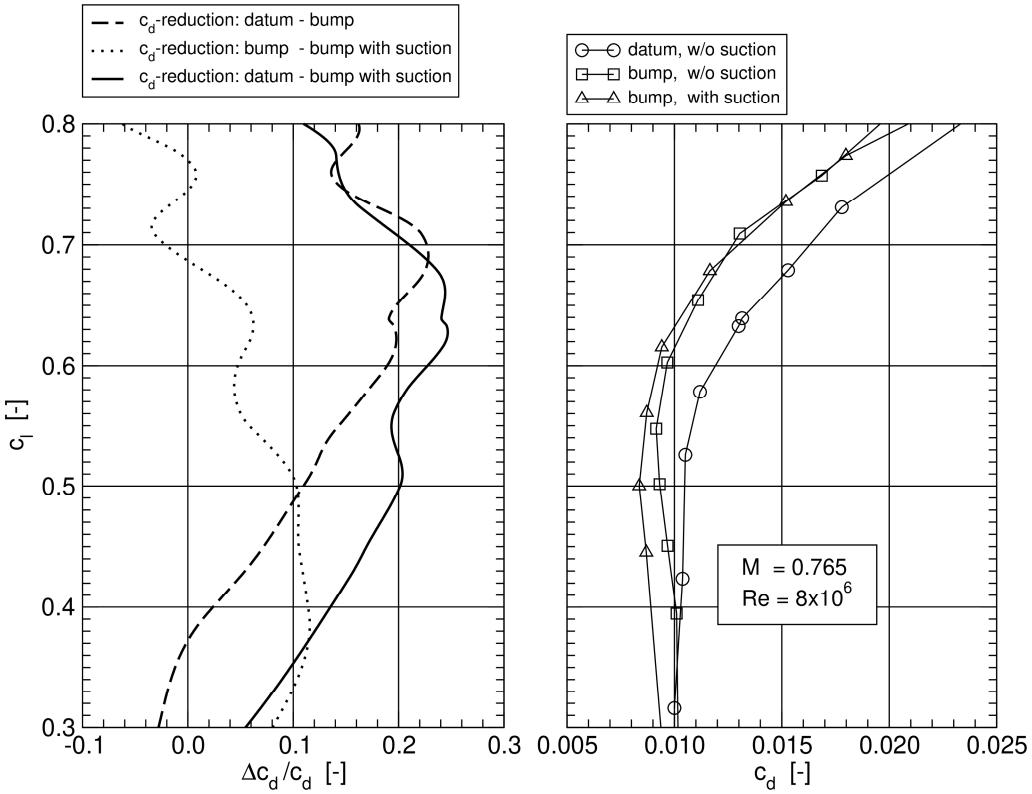

Figure 26: Drag reduction on a transonic airfoil by suction and shock control bump

5.4 Fibre-Based Wind Tunnel Model

The collaborative project "HighART" is dedicated to conducting performance measurements and certification tests for emission-reduced aircraft configurations featuring wings with significantly increased aspect ratio and elasticity, as well as to preparing the corresponding test techniques. Previously, flight performance data has mostly been determined in advance at the ETW, where special steels are typically used for the models due to the cryogenic conditions. Isotropic steel can only replicate the actual lightweight structural wing to a limited extent, so its deformation under load during experiments (specifically bending and torsion) does not accurately match the loads experienced in flight. Due to the increased wingspan and significantly improved efficiency of future concepts, much more flexible wings will be used. Currently, these cannot be simulated accurately to scale, as the available prediction methods are insufficient. HighART builds directly upon the work of the "KoMMod" project (Lemarechal et al., 2023) and employs custom-tailored, fiber-based materials that are optimized for bending and torsion, ensuring the deformation behavior is replicated as faithfully as possible to acquire aerodynamic coefficient data.

Figure 27 shows a CFRP-model installed in the KRG's test section with only the downstream left side clamped at the side wall, while the downstream right side of the model can move freely in a range of 10 mm within the side wall. Within first experiments in the HighART project it was possible to measure the bending and torsion of this model due to the aerodynamic loads and check the predicted deformation as a basis for upcoming experiments at the ETW.

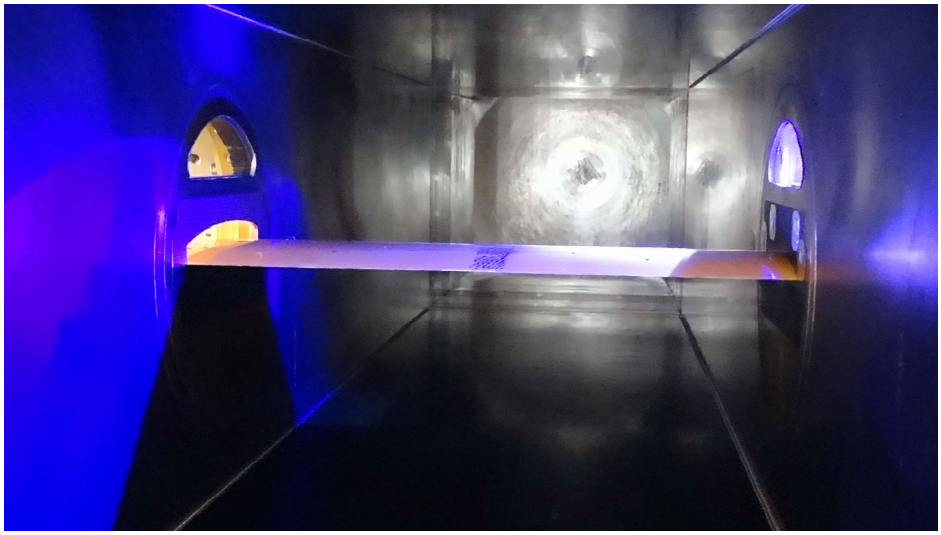

Figure 27: CFRP-model in the KRG, upstream view on the model's trailing edge, one side clamped only

5.5 Defense Related Topics

On highly agile aircraft with swept wings, jet engine air intakes are generally built directly into the fuselage or the wings. This type of integration usually requires the use of non-circular inlets alongside curved diffusers. Additionally, since these intakes are positioned close to the aircraft's wetted surface, it is necessary to account for the boundary layer that develops upstream.

The effect of the ingestion of a boundary layer into high aspect ratio intakes with S-shaped diffusers has been the topic of an experimental study in the KRG (Rein & Koch, 2015). Figure 28 shows a sketch of a flat plate with an intake, mounted into the test section (downstream right side wall is removed).

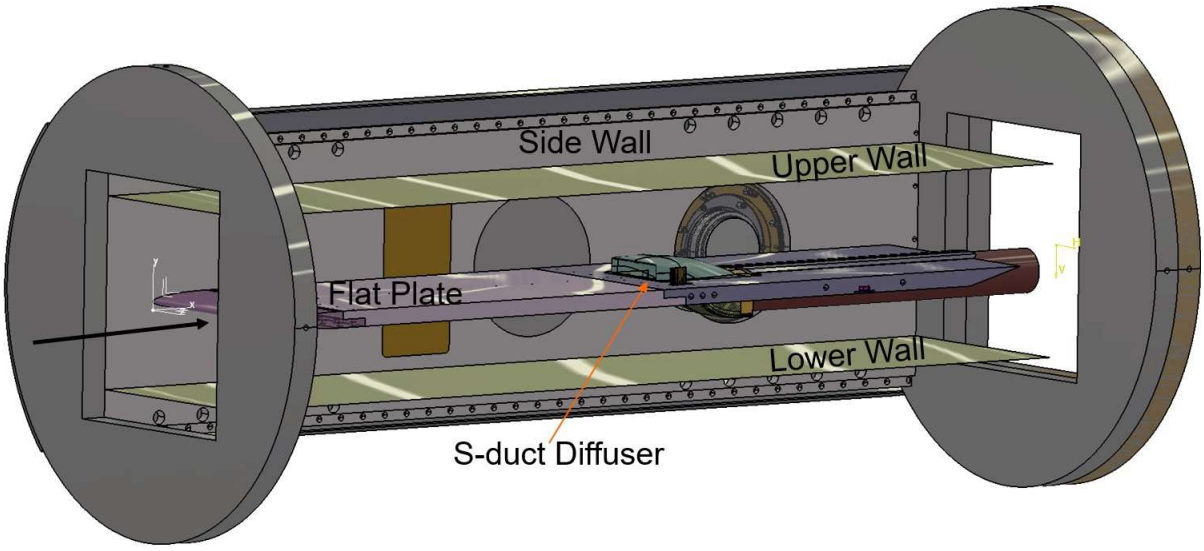

Figure 28: Side view of KRG test section with built-in flat plate with S-duct diffuser

The separation behaviour within the intake and the total pressure distribution at the Aerodynamic Interface Plane (AIP) were investigated. The large domain of Reynolds numbers that can be adjusted at the KRG made it possible to vary the boundary layer thickness in a wide range compared to other facilities. Figure 29, left picture, shows the pressure losses in the AIP due to separation in the S-duct dif-

fuser. Small vortex generators were used to reduce the pressure losses at the AIP (Fig. 29, centre picture).

The ingestion of a bigger vortex into the S-duct diffuser was also part of the test campaigns, simulating a fighter aircraft's leading edge vortex entering the diffusor (Fig. 29, right picture). This data was then compared to numerical studies showing a good qualitative agreement with the experimental results (Koch et al., 2018).

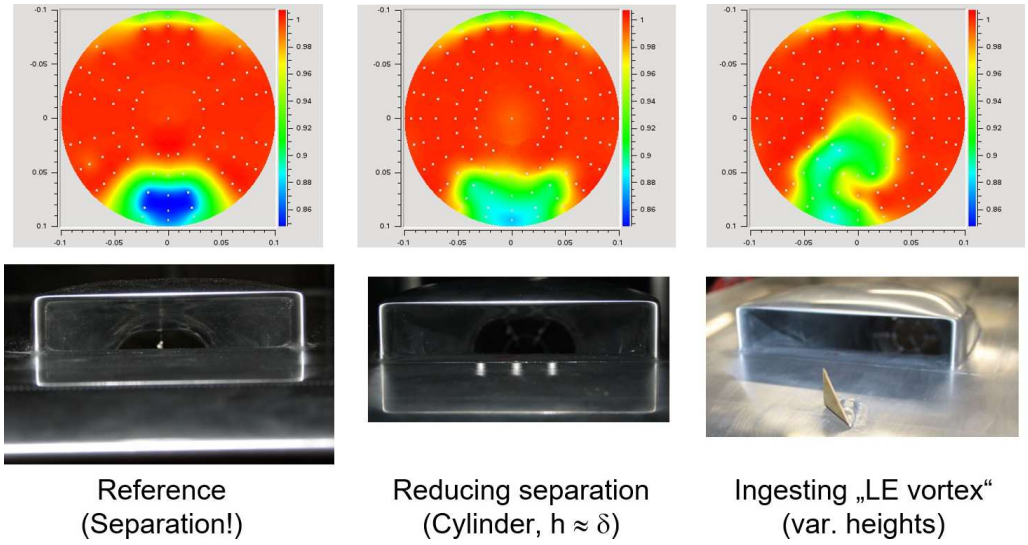

Figure 29: Total pressure losses at the AIP for varying vortex generators

Another defense related topic is weapons bay aerodynamics. The aerodynamic environment of an open weapons bay during high-speed flight is characterized by complex fluid-acoustic interactions, primarily driven by cavity flow resonance. When the boundary layer separates at the leading edge of that cavity, a turbulent shear layer spans the opening and impinges on the trailing edge. This impingement generates acoustic pressure waves that propagate upstream, perturbing the separating shear layer and creating a self-sustaining aeroacoustic feedback loop. The distinct, high-intensity tonal frequencies resulting from this resonance are classified as Rossiter modes. Understanding and mitigating these Rossiter modes is critical, as they induce severe structural fatigue and compromise store separation trajectories.

Experiments in the Cryogenic Ludwieg-Tube Göttingen at flight Reynolds numbers aim at an enhanced insight of the flow above and within weapons bay relevant cavities and corresponding flow control measures. Research on the complex and time-dependent aerodynamics of a weapons bay is done on a flat plate with cavity (Fig. 30) including the application of enhanced optical measurement techniques like iPSP (see Section 4.3) under cryogenic conditions.

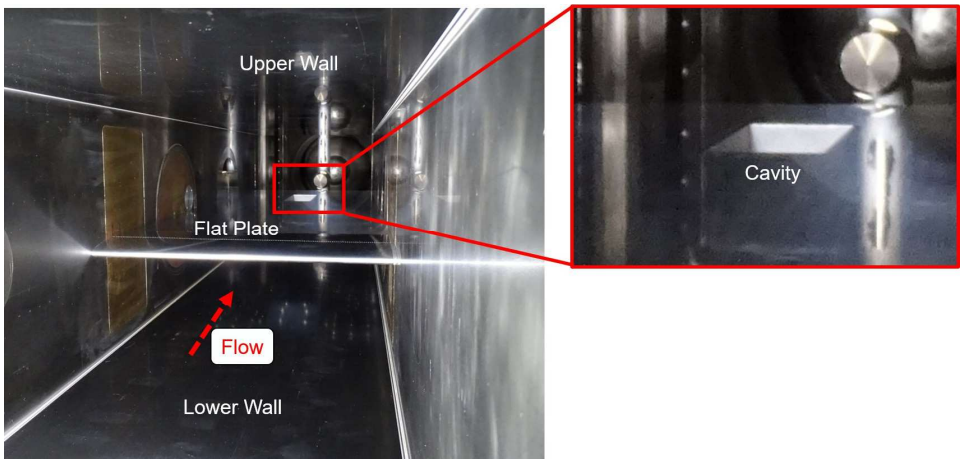

Figure 30: Flat plate with cavity, build in KRG test section, downstream view

6 Conclusion

The Cryogenic Ludwieg-Tube Göttingen (KRG), in conjunction with the European Transonic Windtunnel (ETW), constitutes the exclusive aerodynamic infrastructure in Europe capable of achieving transonic flow at Reynolds numbers representative of full-scale flight conditions for modern transport aircraft. Operated by the German Aerospace Center's (DLR) Institute of Aerodynamics and Flow Technology, the KRG constitutes a critical infrastructure for today's and future aeronautical research.

To achieve flight Reynolds numbers, this facility uses cryogenic temperatures as low as 120 K, together with stagnation pressures of up to 1 MPa. A primary scientific objective of the experimental investigations conducted at the KRG involves aerodynamic drag reduction and advanced flow control for future transport aircraft configurations in the civil sector as well as in the defense domain. This is accomplished through the study of boundary layers and laminarisation techniques, which inherently require precise simulations of realistic flight conditions. By offering a large operational envelope for both Mach and Reynolds numbers, the KRG serves as an essential instrument for the validation of novel aerodynamic design frameworks and computational prediction models. Beyond foundational aerodynamic research, the KRG is a platform for the development of advanced measurement techniques intended for application in other cryogenic wind tunnels, such as the ETW.

References

Amecke, J. (1985). *Direkte Berechnung von Wandinterferenzen und Wandadaptionen bei zweidimensionaler Strömung in Windkanälen mit geschlossenen Wänden* (Forschungsbericht No. DFVLR FB 85-62). Göttingen: DFVLR.

Dimond, B. (2024). *Investigation of boundary layer transition at high reynolds numbers using time-resolved temperature-sensitive paint* (PhD Thesis). Georg-August-Universität Göttingen.

Fey, U., & Egami, Y. (2007). Transition detection by temperature-sensitive paint. In C. Tropea, J. Foss, & A. Yarin (Eds.), *Springer handbook of experimental fluid mechanics* (chap. 7.4). Heidelberg: Springer.

Gardner, A. D. (2007, Februar). *Design and Optimisation of the Valve Contour (Conus) of the DNW-KRG for an extended Mach number Range* (Interner Bericht No. DLR-IB 224 - 2007 A 02). DLR.

Gibson, T., Soucheleau, B., & Rogers, N. (2020). BLADE - Natural Laminar Flow Flight Testing. In *Proceedings of the 32nd congress of the international council of the aeronautical sciences.* Shanghai, China: ICAS. (Available as ICAS2020_0220_paper.pdf on the ICAS archive)

Holst, H. (1991). *Procedure for determination of three-dimensional wind-tunnel wall interferences and wall adaptation in compressible subsonic flow using measured wall pressures* (Forschungsbericht No. DLR FB 91-09). DLR. Retrieved from https://elib.dlr.de/24286/

Hurwitz, R., A. und Courant. (1964). Allgemeine Funktionentheorie und elliptische Funktionen. Springer, Berlin, Göttingen, Heidelberg, New York.

Klein, C. (2022). Time resolved pressure measurements by means of PSP in cryogenic conditions. (AIAA 2022-1938). Retrieved from https://arc.aiaa.org/doi/abs/10.2514/6.2022-1938 http://dx.doi.org/10.2514/6.2022-1938

Klein, C., Yorita, D., Henne, U., Kleindienst, T., Koch, S., & Ondrus, V. (2020, Januar). Unsteady Pressure Measurements by means of PSP in Cryogenic Conditions. In *AIAA Scitech 2020 Forum* (pp. 1–10). AIAA. Retrieved from https://elib.dlr.de/134613/ (AIAA-2020-0122)

Koch, S. (2004). *Zeitliche und räumliche Turbulenzentwicklung in einem Rohrwindkanal und deren Einfluss auf die Transition an Profilmodellen* (Forschungsbericht No. DLR FB 04-19). DLR.

Koch, S. (2020). *Druckverteilungsmessungen zum Einfluss von Absaugung auf das Profil ADIF mit Konturbeule im DNW-KRG* (Tech. Rep. No. DLR-IB-AS-GO-2020-47). Deutsches Zentrum für Luft- und Raumfahrt e.V. Retrieved from https://elib.dlr.de/134737/

Koch, S., Rütten, M., & Rein, M. (2018). Study of total pressure losses at the engine face of a submerged inlet with an ingested vortex. In A. Dillmann et al. (Eds.), *New results in numerical and experimental fluid mechanics xi* (Vol. 136, pp. 361–371). Springer. Retrieved from https://elib.dlr.de/117262/ (ISSN 1860-0824)

Lemarechal, J., Koch, S., Klein, C., & Koop, L. (2023). *Schlussbericht zum LuFo 5 Vorhaben KoMMod-DLR "Transitionsmesstechniken für Karbonfaser-Modelle in industrie-relevanten Windkanälen"* (DLR-Interner Bericht No. DLR-IB-AS-GO-2023-77). Retrieved from https://elib.dlr.de/197065/

Ludwieg, H. (1955). Der Rohrwindkanal. *Z. Flugwiss.*, *3*(7), 206–216.

Rein, M., & Koch, S. (2015). Experimental study of boundary-layer ingestion into a diverterless s-duct intake. *AIAA Journal*, *53*(11), 3487–3491. Retrieved from https://elib.dlr.de/99028/ http://dx.doi.org/10.2514/1.J053902

Risius, S., Costantini, M., Koch, S., Hein, S., & Klein, C. (2018). Unit Reynolds number, Mach number and pressure gradient effects on laminar-turbulent transition in two-dimensional boundary layers. *Experiments in Fluids*, *59*(5), 1–29. Retrieved from https://elib.dlr.de/122349/ http://dx.doi.org/10.1007/s00348-018-2538-8

Rosemann, H. (1996, 20–24 May). The Cryogenic Ludwieg-Tube at Göttingen [Report]. In *Special course on advances in cryogenic wind tunnel technology.* (Cologne, Germany).

Schülein, E., Koch, S., & Rosemann, H. (1998, 22–25 September). Skin friction measurement and transition detection techniques for the Ludwieg-Tubes at DLR [Conference Proceeding]. In *Advanced aerodynamic measurement technology.* (Seattle, United States).

Steinle, F. W., & Stanewsky, E. (1982). Wind tunnel flow quality and data accuracy requirements..